Bifunctional CoFeVO$_x$ Catalyst for Solar Water Splitting by using Multijunction and Heterojunction Silicon Solar Cells

Minoh Lee,* Xinyu Ding, Swarnendu Banerjee, Florian Krause, Vladimir Smirnov, Oleksandr Astakhov, Tsvetelina Merdzhanova, Benjamin Klingebiel, Thomas Kirchartz, Friedhelm Finger, Uwe Rau, and Stefan Haas

Photovoltaic driven electrochemical (PV-EC) water splitting technology is considered as one of the solutions for an environmental-friendly hydrogen supply. In a PV-EC system, efficient catalysts are required to increase the rate of both oxygen evolution reaction (OER) and hydrogen evolution reaction (HER). Here, the development of a CoFeVO$_x$ bifunctional catalyst produced by a simple electrodeposition method is presented. It is found that after the water splitting reaction, vanadium is almost completely depleted in the mixture of elements for OER, while its concentration at the HER catalyst is similar or even higher after the reaction. For the OER catalyst, the depletion of vanadium might lead to the formation of pores, which could be correlated with the activity enhancement. The developed catalyst is integrated into PV-EC devices, coupled with different types of silicon PV. An average solar to hydrogen efficiency of 13.3% (9.6 cm^2 PV aperture area) is achieved with a shingled module consisting of three laterally series-connected silicon heterojunction solar cells.

1. Introduction

Water electrolysis operated with renewable energy is considered to be an environmental-friendly approach for hydrogen production.[1] The hydrogen can be used as energy storage medium[2] or as industrial raw material, for example, in climate neutral steel production.[3] Photovoltaic (PV) driven water electrolysis

is one of the pathways among three different solar driven hydrogen production approaches (i.e., photocatalyst,[4] photoelectrochemical,[5] PV[6]), where the PV part as power supply can be directly connected to the electrochemical (EC) part.[7] Although water electrolysis can be operated in any pH condition, efficient and stable catalysts made of earth-abundant materials are mostly found for strong alkaline electrolytes.[8] Among the promising candidates in alkaline electrolysis, inorganic Co-based compounds have been intensively investigated due to their reasonable performance.[9,10] Iron is relatively well known as a dopant in the Co-based catalysts, and the activity of Fe-doped Co catalysts is significantly enhanced by synergistic effects between Co and Fe.[11] Recently, it was found that the incorporation of high-valence vanadium (V) in Co-based

catalysts is beneficial for the oxygen evolution reaction (OER) performance.[12] It is suggested that V doping may play a role in adjusting the electronic structure in the Co-based catalysts. In order to increase the activity of the OER catalysts also ternary Co—V—Fe compounds have been prepared and investigated.[13]

We have investigated the use of different Co-based catalysts in bifunctional configuration. A bifunctional configuration (one type of the catalyst for both, anode and cathode at the same time) offers a great potential for reducing the cost of catalyst production and thus of the entire system.[14] The composition of the binary and ternary catalysts was adjusted according to the metal-hydroxide (M—OH) bond strength theory.[12a,15] Each type of mixed compound was explored in both OER and hydrogen evolution reaction (HER) in the same alkaline electrolyte. We found that the sample consisting of Co$_{0.6}$Fe$_{0.3}$V$_{0.1}$O$_x$ shows the best performance (at 10 mA cm^{-2}) with an overpotential of 269 mV for HER and 266 mV for OER, respectively. An X-ray photoelectron spectroscopy (XPS) analysis has revealed that vanadium is almost completely depleted in the OER catalyst after the reaction. In combination with the Pourbaix diagram of V species, we assume that for OER vanadium does not modify the electrical property,[13b] the M—OH binding energy,[12a] or the coordination environment in the mixed film[12b,16] as previously suggested. Probably the dissolution of the vanadium results in the creation of pores in the mixed catalyst that might be related to the positive

Dr. M. Lee, X. Ding, S. Banerjee, F. Krause, Dr. V. Smirnov,
Dr. O. Astakhov, Dr. T. Merdzhanova, Dr. B. Klingebiel,
Prof. T. Kirchartz, Dr. F. Finger, Prof. U. Rau, Dr. S. Haas
IEK5 – Photovoltaik
Forschungszentrum Jülich GmbH
Jülich 52425, Germany
E-mail: m.lee@fz-juelich.de, molee0422@gmail.com
Prof. T. Kirchartz
Faculty of Engineering and CENIDE
University of Duisburg-Essen
Carl-Benz-Str. 199, Duisburg 47057, Germany

The ORCID identification number(s) for the author(s) of this article can be found under https://doi.org/10.1002/admt.202000592.

effects on the OER activity.[17] Importantly, this result means that the "M−OH bond strength theory" may not be applied to all metals as an experimental design guidance. The bifunctional $Co_{0.6}Fe_{0.3}V_{0.1}O_x$ catalyst was integrated into Photovoltaic driven electrochemical (PV-EC) devices together with different types of silicon-based PV cells (triple-junction a-Si:H/a-Si:H/μc-Si:H solar cells and a shingled module consisting of three series-connected silicon heterojunction (SHJ) solar cells; hereafter denoted as the shingled module). The initial solar to hydrogen (STH) efficiency was found to be 7.6% for the triple-junction thin-film Si approach and 13.5% for the device using the shingled module.

2. Result and Discussion

2.1. Design of Bifunctional Electrocatalyst by Means of Metal Hydroxide (M−OH) Bond Strength Theory

The development of a theoretical description of surface reactions on metal-based catalysts has attracted great attention from many research groups.[18] Accurate activity descriptors can be a useful experimental guide to identify an optimal catalyst. Although there are still some questions on how to predict an efficient electrochemical water splitting catalyst in alkaline electrolytes, in many cases the metal-hydrogen (M−H) bond strength for the HER and the metal-hydroxide (M−OH) bond strength for the OER are considered significant descriptors.[8] Here, we have used the M−OH bond strength instead of the M−H bond strength in the development of the bifunctional catalyst because OER is generally considered to be the bottleneck process in electrochemical water splitting systems due to its slow kinetics involving a four-electron process compared to the counterpart of HER with a two-electron process.[19]
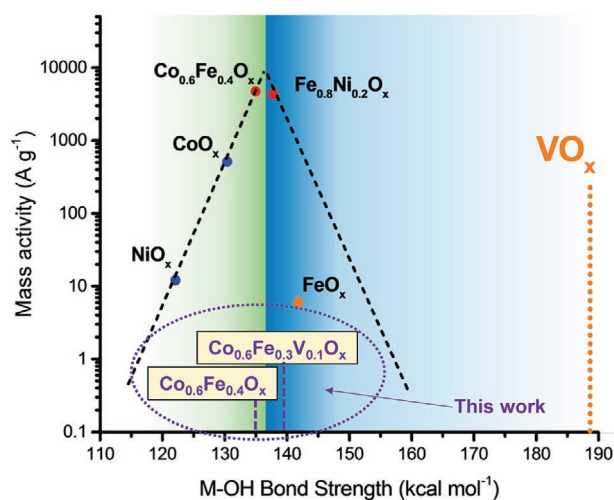

Figure 1. Volcano plot of mass activity for OER as a function of M−OH bond strength. The M−OH bond strength of two samples prepared in the current study near the optimal value for the mass activity (137 kcal mol⁻¹) is exemplarily shown (dashed purple lines). The purple dotted oval represents the range of M−OH bond strengths investigated in the current study. Note that the values of our samples are only correlated to M−OH bond strength in x-axis, not for mass activity in y-axis. This figure is compiled on the basis of the data given from ref. [12a] (Figure 1). Reused with permission from ref. [12a]. Copyright, ACS Catal. 2018, 8, 644–650.

For a series of Co-based mixed catalysts we have calculated the M−OH bond strength based on the data previously published by Bockris and Otagawa (see Table S1, Supporting Information).[20] The volcano plot of mass activity versus M−OH bond strength is represented in **Figure 1**. This graph is compiled based on the data given by Liardet and Hu.[12a] Several 3d metal oxide catalysts and mixed-metal oxide catalysts are predicted with their mass activity and M−OH bond strength in the volcano plot. The maximal mass activity is expected at a bond strength of 137 kcal mol⁻¹. The M−OH bond strength of CoO_x is calculated to be 130.4 kcal mol⁻¹, positioning in the left branch of volcano plot, whereas FeO_x is located in the right branch of the plot with a bond strength of 141.8 kcal mol⁻¹. The bond strength of VO_x is shown to be 188.5 kcal mol⁻¹, which is located on the far right side in the plot. As shown in Figure 1, two kinds of mixed catalysts (i.e., $Co_{0.6}Fe_{0.4}O_x$ with 135 kcal mol⁻¹ and $Co_{0.6}Fe_{0.3}V_{0.1}O_x$ with 139.6 kcal mol⁻¹) are positioned near the optimal peak (137 kcal mol⁻¹) suggested by Liardet and Hu.[7a] These two catalysts might be beneficial for OER, and highlighted by the purple dotted oval. Notably, the values of our samples are only correlated with M−OH bond strength shown on the x-axis, not for mass activity shown on the y-axis.

2.2. Realization of an Electrodeposited Bifunctional CoFeVO_x Water Splitting Catalyst

In **Figure 2**a,b, the overpotentials of all prepared samples are compared for HER and OER, respectively. To precisely evaluate overpotential values, chronopotentiometry measurements were conducted with three samples each. The values were extracted at a current density of 10 mA cm⁻² after initial stabilization. In case of HER (Figure 2a), the overpotential gradually decreases with an increasing Fe content in the mixed film. Although $Co_{0.6}Fe_{0.4}O_x$ shows the best average performance for HER of three samples (288.7 ± 8.3 mV), it is still worth mentioning that the best individual sample was found in the batch of $Co_{0.6}Fe_{0.3}V_{0.1}O_x$ (269 mV). Similarly, for OER the average overpotential decreases with an increasing Fe content up to 30% ($Co_{0.6}Fe_{0.3}V_{0.1}O_x$). However, further increase of the Fe content ($Co_{0.6}Fe_{0.4}O_x$) has negative effect on the OER performance. This trend in the OER performance quite similarly comes into line with the prediction by M−OH bond strength. A stability test was carried out with the $Co_{0.6}Fe_{0.3}V_{0.1}O_x$ sample by tracking the applied voltage at a constant current density of 10 mA cm⁻². The corresponding overpotentials of HER and OER are given in Figure 2b. The overpotentials first gradually decrease and reach steady-state conditions after ≈30 min. This stabilization is perhaps correlated to the dissolution of V (for OER, will be discussed in the following section) and a rearrangement (e.g., redox reaction, dissolution, electromigration) of the catalyst surface.[21] They are maintaining stable within 2 h.

2.3. Role of Vanadium in Co_{0.6}Fe_{0.3}V_{0.1}O_x Catalyst: A Forgotten Pourbaix Diagram

In order to test for relative compositional changes of $Co_{0.6}Fe_{0.3}V_{0.1}O_x$ after the water splitting reaction, XPS analysis

ADVANCED
SCIENCE NEWS
www.advancedsciencenews.com

ADVANCED
MATERIALS
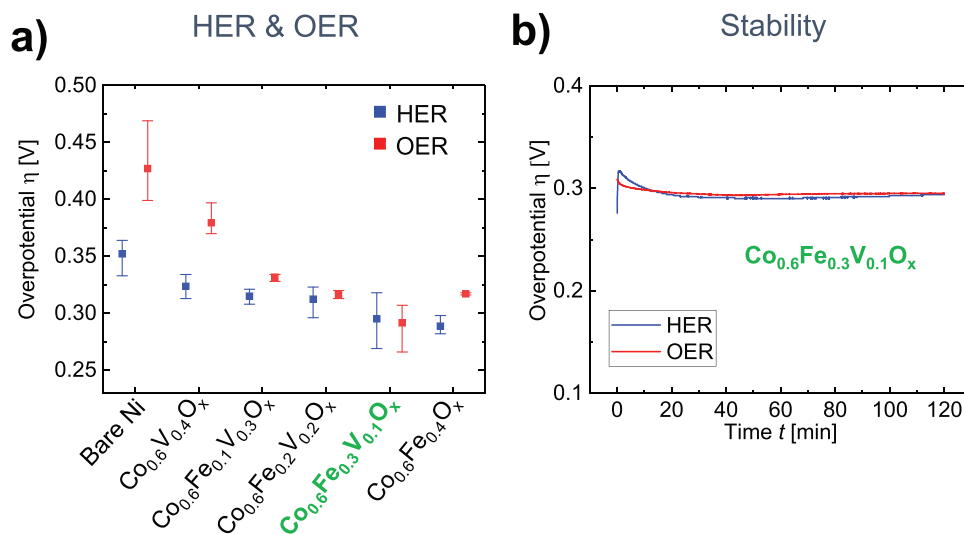TECHNOLOGIES
www.advmattechnol.de

Figure 2. Electrochemical characterization of the electrodeposited Co-based mixed catalysts. a) Overpotential of HER and OER for the different catalysts studied. The measurements were conducted with three samples each (size 1.2 cm × 4.6 cm) in 1 M KOH at ambient condition. The values of overpotential were extracted from chronopotentiometry plots at a constant current density of 10 mA cm^{-2} after reaching steady-state conditions. b) Electrocatalytic chronopotentiometry measurement for 2 h with the $Co_{0.6}Fe_{0.3}V_{0.1}O_x$ sample.

was employed (**Figure 3**). In the XPS spectra of Co 2p, shown in Figure 3a, two main peaks for Co 2$p_{3/2}$ and Co 2$p_{1/2}$ are located at 781.2 and 797.3 eV in the as-prepared sample (red line).[22] The peak intensity increased significantly after OER while it remained similar after HER. Notably, the Co^{2+} peak placed near 797.3 eV was shifted to lower energies after OER, which indicates a relative oxidation of Co^{2+} species to Co^{3+}. This is consistent with previous results from the literature.[13b] In the case of Fe 2p, which is shown in Figure 3b, two peaks for Fe 2$p_{3/2}$ and Fe 2$p_{1/2}$ appeared near 711 and 725 eV.[22] Here, no significant changes were observed after the water splitting reaction. Interestingly, the signal near 517 eV in the V 2$p_{3/2}$ spectra[23] (Figure 3c) disappeared after OER while the relative ratio of vanadium to oxygen increases after HER (from 0.06 to 0.17).

The concentration of vanadium in the catalyst was qualitatively investigated by means of scanning electron microscopy (SEM) and the corresponding energy-dispersive X-ray spectroscopy (EDX) analysis. Figure S6, Supporting Information shows a comparison of the $Co_{0.6}Fe_{0.3}V_{0.1}O_x$ catalyst composition before and after water splitting. The different EDX spectra only show very little variations. The vanadium peak is slightly decreased after OER, but does not completely disappear. However, this result is no proof that vanadium is still present on the surface, since EDX has a relatively large penetration depth (1–3 μm[25]) compared to XPS (5 nm[26]). To support the V dissolution hypothesis in OER, we prepared a sample having a higher composition of V ($Co_{0.6}V_{0.4}O_x$). The intensity of the EDX V peak was much higher in the as deposited state compared to the previous sample ($Co_{0.6}Fe_{0.3}V_{0.1}O_x$, see Figures S6a and 7a, Supporting Information). After OER, the intensity of V peak was severely reduced. This implies that V is not stable during OER (see EDX spectrum in Figure S7b, Supporting Information).

The dissolution of V is supported by the Pourbaix diagram (E–pH), which can be very helpful to elucidate the inorganic solution chemistry of the various chemical elements. This diagram, however, has not been much considered as guidance in

the water splitting field to date. **Figure 4** shows the different vanadium species as a function of pH value (x-axis) and voltage with respect to the standard hydrogen electrode (SHE; y-axis). The red dashed box placed on the right side in Figure 4 indicates the region where water splitting occurs (pH: ≈13.6). The black dashed diagonal lines over the whole pH range represent OER (upper dashed line) and HER (lower dashed line), respectively. The dashed lines are drawn according to the equilibrium potentials (E_{eq}) listed below, which are determined on the SHE scale.

$$HER : E_{eq}\,(V) = -0.059\,V \times pH \tag{1}$$

$$OER : E_{eq}\,(V) = -0.059\,V \times pH + 1.23\,V \tag{2}$$

Note that the E_{eq} shifts with varying pH while the potential difference between OER and HER stays constant at 1.23 V for any pH value.[27] The Pourbaix diagram shows that vanadium is present in the ionic state (VO_4^{3-}) under OER conditions, while it is in a solid state (V_2O_3 phase) under HER conditions. That means, vanadium is thermodynamically unstable for OER conditions at high pH values and can be dissolved from the anode ($Co_{0.6}Fe_{0.3}V_{0.1}O_x$) into the electrolyte. This is consistent with the measured XPS spectra of V 2p (cf. Figure 3c). However, the Pourbaix diagram was not considered in the previous studies,[12,13,16,28] thereby they concluded the synergetic effects by vanadium doping as a reason of enhancement of OER activity. Although they proved the existence of V, mostly original (as-prepared) samples were considered for the prediction and experiments. Also, possibly the samples might be investigated after precipitation of V (or intermediate/internal migration state prior to dissolution) during the in-situ and ex-situ measurements (after OER). V can also remain in the catalyst after OER because the inner part of catalysts can be impermeable to the electrolytes from the barrier of evolved gases/ or mass transfer limitation. In contrast to the explanations of the synergetic effects by vanadium doping, we assume that the
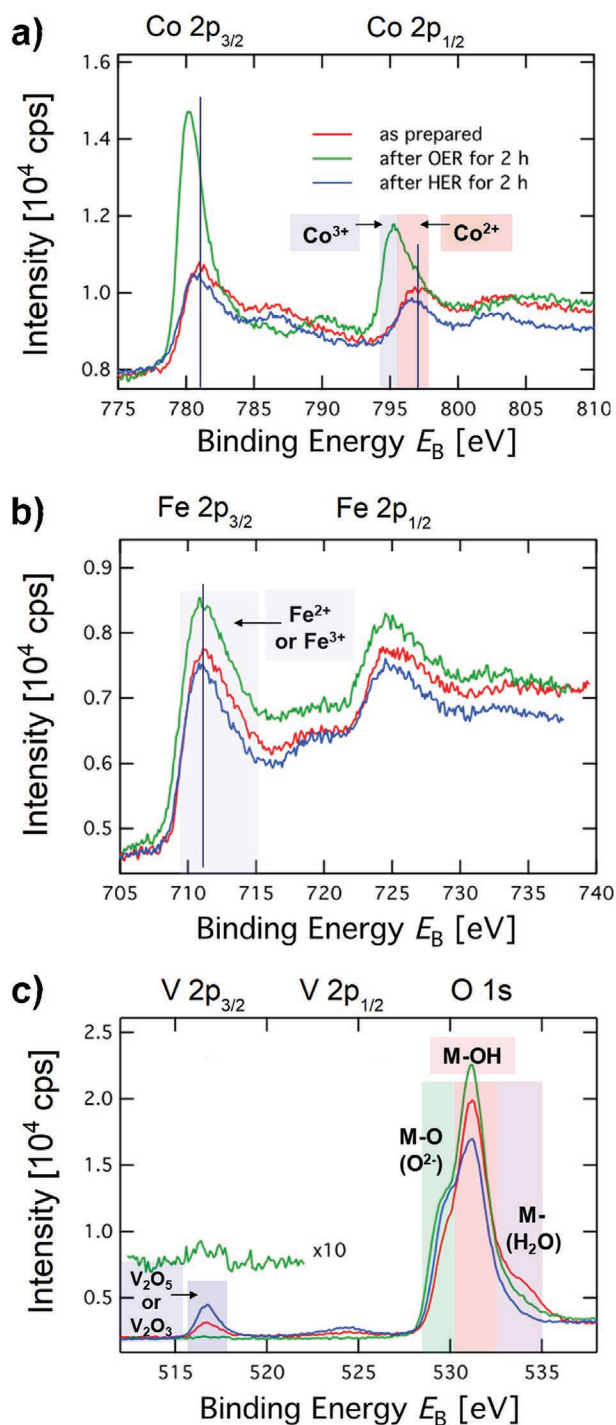
2000592 (3 of 9)

**ADVANCED
SCIENCE NEWS**
www.advancedsciencenews.com

**ADVANCED
MATERIALS
TECHNOLOGIES**
www.advmattechnol.de

Figure 3. Investigation of the $Co_{0.6}Fe_{0.3}V_{0.1}O_x$ catalyst by XPS analysis. XPS spectra of a) Co 2p, b) Fe 2p, c) V 2p and O 1s of $Co_{0.6}Fe_{0.3}V_{0.1}O_x$ before and after water splitting reaction.

improvement of OER activity by increasing the amount of vanadium in the catalyst ($Co_{0.6}Fe_{0.3}V_{0.1}O_x$) could be related to the formation of pores that are created by the dissolution of vanadium from the mixed film.[17] However, further in-depth investigations are required to explore the exact mechanisms.

2.4. Integration of Catalyst into PV-EC Devices

We either used PV cells (or modules) with a vertically integrated multijunction structure or a laterally series-connected structure to provide the voltage (>1.6V) required for the realization of spontaneous (bias-free) PV-EC devices.[29] In this study, three different types of Si PV (a-Si:H/a-Si:H/μc-Si:H thin-film cells, a-Si:H/μc-Si:H/μc-Si:H thin-film cells, and the shingled module consisting of three series-connected SHJ solar cells) were prepared for the integration in three different device configurations. In all devices the $Co_{0.6}Fe_{0.3}V_{0.1}O_x$ mixed catalyst was chosen since it offers the lowest total overpotential (calculated by sum of each half reaction) among all investigated $CoFeVO_x$ catalysts. Even though the error deviation of the $Co_{0.6}Fe_{0.3}V_{0.1}O_x$ catalysts for both OER and HER is shown to be larger than for other catalysts, the overpotential of $Co_{0.6}Fe_{0.3}V_{0.1}O_x$ shows the lowest value even at the worst case for OER, and shows comparable values for HER. The different devices are compared to each other and to literature values as well (see Table S3, Supporting Information).

Figure 5a shows a schematic image (inset; optical photography) of the type I PV-EC device, which consists of triple-junction thin-film silicon solar cells as power source and $Co_{0.6}Fe_{0.3}V_{0.1}O_x$ as catalyst for water electrolysis. The PV part (1.5 cm^2 active area), which is completely separated from the electrolysis reaction chamber (Figure S11, Supporting Information), is connected to the EC part (catalysts each 1.85 cm^2 active area) by a pin-contact. A cross-sectional schematic image (Figure 5b) of an integrated PV-EC device (type I) is given, and the respective I–V characteristics of the PV part and the EC part are shown in Figure 5c. The I–V characteristic of the EC part was drawn in reverse direction with respect to the voltage axis in order to find the intersection point, where both I–V curves of PV and EC meet. In general, the intersection point can be considered to be the operation current of the integrated PV-EC device under unbiased conditions. In case of the a-Si:H/a-Si:H/μc-Si:H cells, the operation current was expected to be $I_{op,pre}$ = 8.76 mA, which is much higher than the expected operation current of the configuration using the a-Si:H/μc-Si:H/μc-Si:H PV cells (I = 0.70 mA).

Even though a-Si:H/μc-Si:H/μc-Si:H solar cells have a higher short circuit current J_{sc} than the a-Si:H/a-Si:H/μc-Si:H solar cells, the photovoltage of the former type of cells is not sufficient for an efficient spontaneous operation. Therefore, we selected a-Si:H/a-Si:H/μc-Si:H PV cells as power source for the integrated PV-EC device (type I). As shown in Figure 5d, the operation current of an integrated PV-EC device was monitored (left y-axis) for 2 h under 1 sun of AM1.5G illumination intensity without assistance of additional bias. The operation current was I_{op} = 8.88 mA at the beginning of the measurement, which is close to the predicted value from the intersection point (8.76 mA). The operation current continuously decreased with time and finally reached I_{op} = 6.78 mA. In order to investigate the reason for the significant operation current decrease, we monitored the current density of a-Si:H/a-Si:H/μc-Si:H cell at maximum power point V_{mpp} (1.75 V), which is generally close to the operation voltage in the integrated PV-EC water splitting device. Here, a strong decrease of the current is observed for the 40 h operation time (cf. Figure S12a,
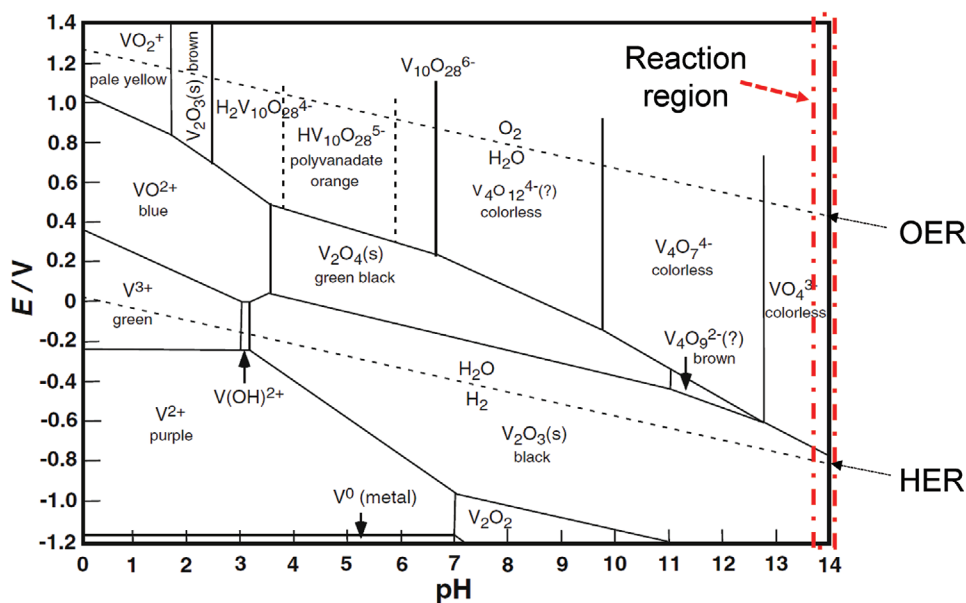
**ADVANCED
SCIENCE NEWS**
www.advancedsciencenews.com

**ADVANCED
MATERIALS
TECHNOLOGIES**
www.advmattechnol.de

Figure 4. Pourbaix diagram of V species compiled from the data given in ref. [24] (Figure 1.20 in page 19). Reproduced with permission.[24] Copyright 2012, Springer.

Supporting Information). Additionally, we also compared the *I–V* characteristic of a separate a-Si:H/a-Si:H/μc-Si:H cell after preparation, after 40 h continuous illumination and after an additional resting time of 5 min without illumination (cf. Figure S12c, Supporting Information). The current density of the solar cell at V_{mpp} 1.75 V decreases significantly after 40 h of operation (≈54% decrease; from 6.45 to 2.95 mA cm^{-2}), mainly due to a decrease of the open circuit voltage V_{oc}, while the short circuit current density J_{sc} is much less affected (from 7.41 to 7.35 mA cm^{-2}). The decrease of the V_{oc} upon a temperature increase in similar a-Si:H/a-Si:H/μc-Si:H device structures as used in the present study has been investigated recently.[30] Based on the strong difference between the current densities at short circuit (J_{sc}) and at V_{mpp}, STH efficiency loss would not be closely correlated with solar to electricity efficiency loss. After 5 min without illumination, the current density at 1.75 V was partially recovered. This temperature induced "metastability" indicates how the a-Si:H/a-Si:H/μc-Si:H PV used here is very sensitive to the temperature or a mixture of temperature and bias (especially to the V_{oc} in the device). Therefore, we must be cautious to precisely measure the STH efficiency of a-Si:H/a-Si:H/μc-Si:H-based integrated PV-EC water splitting devices. Details of the measurement conditions such as illumination intensity and time, self-healing of PV due to the preparation time for the measurements; mounting PV to holder, refilling the electrolyte, and connecting electrical line etc. can affect the real temperature of the solar cell which in turn can significantly influence the performance of the integrated PV-EC device.

In order to verify our assumption of temperature dependent degradation, we prepared an integrated PV-EC device (type II) composed of the a-Si:H/a-Si:H/μc-Si:H PV and the Co$_{0.6}$Fe$_{0.3}$V$_{0.1}$O$_x$ catalyst. Contrary to the PV-EC device (type I), the PV is positioned in the electrolyte for better thermal contact. The schematic cross-sectional view of the PV-EC device

(type II) is represented in **Figure 6**a. Corresponding photographs with back side view (EC side) and front side view (PV side) are shown in Figure 6b,c, respectively. The operation current of the PV-EC device was measured for 2 h (Figure 6d). The operation current was quite stable for the first (below ≈1% loss; from −3.11 to −3.08 mA) and the second (≈2.6% loss; from −3.08 to −3 mA) hour of operation. The reason of the decrease in current density after around 80 min might be due to the bubbles effect (attached—decrease in current, detached—increase in current).[31] Noticeable is a clear difference in performance between the PV-EC devices (type I and type II), depending on where the PV device is located, which supports our assumption regarding the importance of thermal coupling for the a-Si:H/a-Si:H/μc-Si:H PV-powered water electrolysis devices.

In order to achieve higher STH efficiencies, we finally prepared a PV-EC device (type III) where three series-connected SHJ solar cells were combined to the shingled module and connected to the Co$_{0.6}$Fe$_{0.3}$V$_{0.1}$O$_x$ bifunctional catalyst. SHJ solar cells give already higher solar to electricity efficiencies compared to triple-junction thin-film silicon solar cells (here ≈20.3% compared to ≈11% of type I and type II devices). However, they cannot supply enough photovoltage with only one cell. Thus, we used a series connection of three cells for water splitting. The PV module, which is positioned outside of the EC part, is connected to the catalysts with an electrically conductive wire (see the schematic illustration in **Figure 7**a). Figure 7b shows the operation current I_{op} of the PV-EC device for 2 h. The device exhibits a quite stable operation with an average operation current of −103.92 mA within the 2 h, which corresponds to an STH efficiency ≈13.3%. Although the STH efficiency is not a record value compared to literature, the result is a promising demonstration among SHJ powered water splitting devices of this size (PV: 9.6 cm^2) utilizing an earth-abundant bifunctional catalyst.
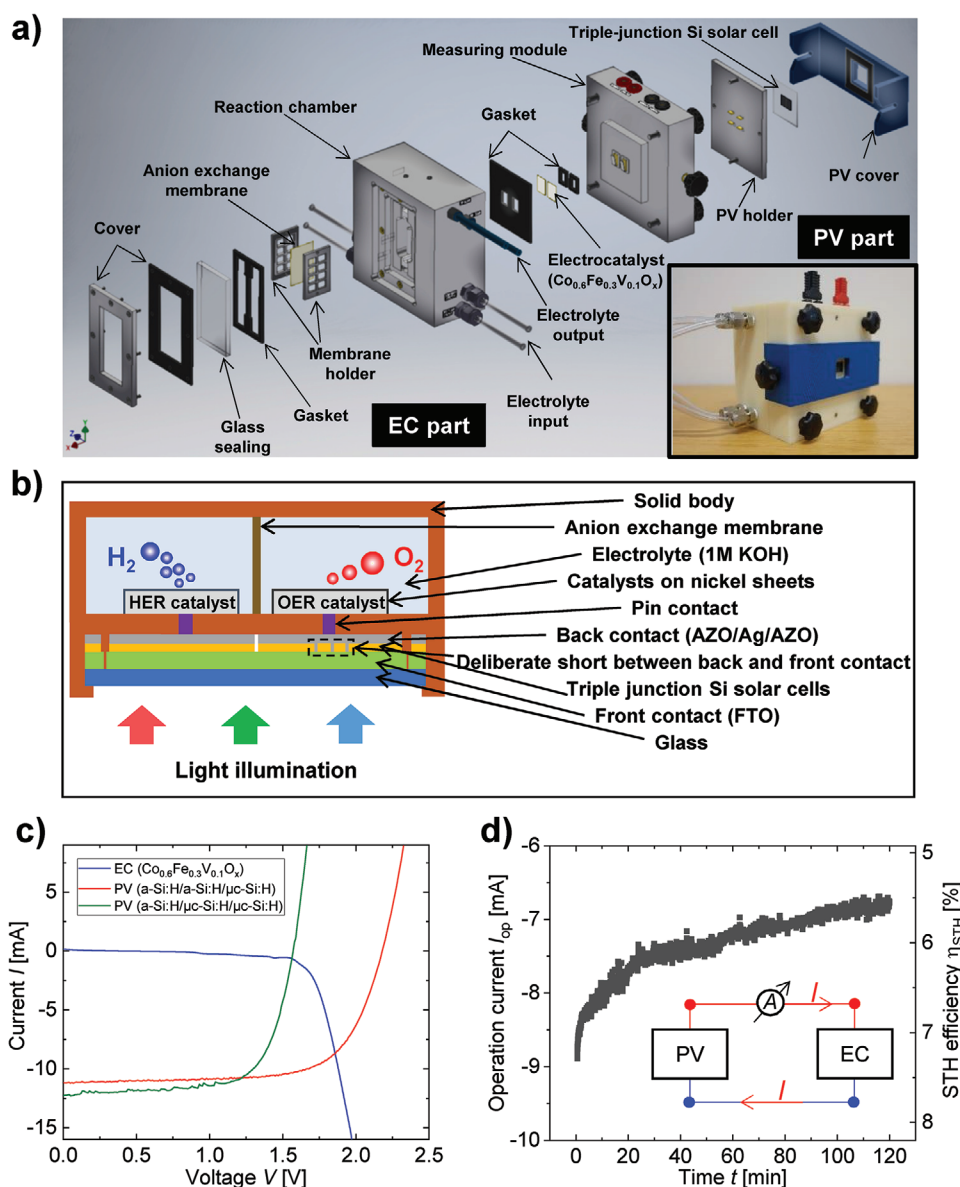
Figure 5. Characterization of an integrated PV-EC device (type I) where the PV part is completely separated from the electrolyzer part with a distance of 3 cm, but integrated into the same scaffold (PV: 1.5 cm² active area, EC: both 1.85 cm²). a) The part assembly drawing (inset shows the image after assembly), b) the schematic cross-sectional view of the PV-EC device. The term "AZO" and "FTO" represent aluminum-doped ZnO (ZnO:Al) and fluorine-doped tin oxide (SnO₂:F), respectively.[33] c) I–V characteristics of PV (two different types of triple-junction Si solar cells; a-Si:H/a-Si:H/μc-Si:H and a-Si:H/μc-Si:H/μc-Si:H) under AM1.5G illumination and EC cell measured in a two-electrode configuration. d) Operation current (left y-axis) and corresponding STH efficiency (right y-axis) of PV-EC device as a function of time under unbiased ($V = 0$ V) condition. Triple-junction Si solar cell (a-Si:H/a-Si:H/μc-Si:H PV: 1.5 cm²) as power source and $Co_{0.6}Fe_{0.3}V_{0.1}O_x$ (EC: 1.85 cm²) as electrocatalysts for water splitting were used. The faradaic efficiency was assumed to be 100%. All the experiments were carried out under 1 sun of AM1.5 illumination intensity in 1.0 M KOH at room temperature.

3. Conclusion

In the present study, a series of Co-based bifunctional catalysts were successfully prepared by electrodeposition. The metal-hydroxide (M—OH) bond strength theory was used to design the mixed metal catalyst films. The $Co_{0.6}Fe_{0.3}V_{0.1}O_x$ sample showed the lowest overpotentials of 269 and 266 mV (at 10 mA cm⁻²) for HER and OER, respectively. According to

the XPS analysis, vanadium is strongly depleted after OER. This result is in contradiction with previous studies where synergetic effects by vanadium doping were proposed as a reason for the enhancement of OER activity by vanadium incorporation. Together with the Pourbaix diagram of vanadium species, we conclude that the depletion of vanadium might lead to the formation of pores, which could be a factor to improve OER performance. It is worth emphasizing that our work proposes
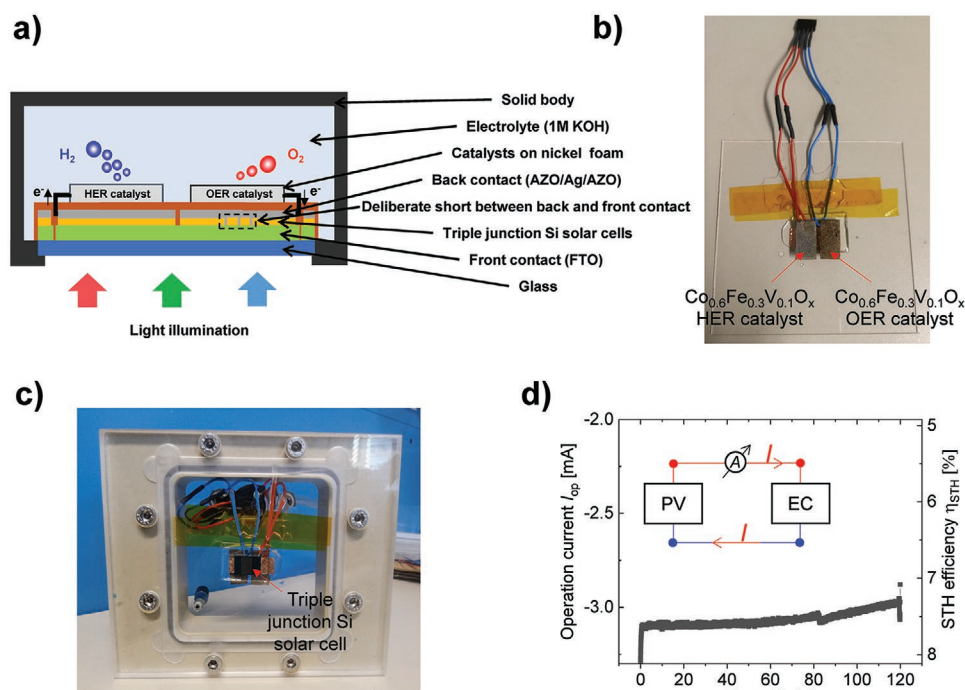
Figure 6. Integrated PV-EC device (type II), where the PV cell is immersed in the electrolyte for cooling purposes (PV: 0.5 cm² active area, EC: both 2 cm²). a) The schematic cross-sectional view of the PV-EC device (type II), and the corresponding photographs. b) Back side view (EC side) and c) front side view (PV side). d) Chronoamperometry measurement (left y-axis) and corresponding STH efficiency (right y-axis) of integrated PV-EC device (type II) as a function of time under unbiased ($V = 0$ V) condition. Triple-junction Si solar cell (a-Si:H/a-Si:H/μc-Si:H PV: 0.5 cm²) and $Co_{0.6}Fe_{0.3}V_{0.1}O_x$ (EC: 2 cm²) were used for spontaneous water splitting. The faradic efficiency was assumed to be 100%. The experiment was carried out under 1 sun of AM1.5 illumination intensity in 1.0 M KOH at room temperature.

the change of the prevailing view of addition of V as a dopant, and the more important message would be that the "metal-hydroxide (M−OH) bond strength theory" might not be applied to all metals as an experimental design guidance.

Three different types of PV-EC device were developed. The first concept is based on triple-junction thin-film silicon solar cells completely separated from the electrolyzer part (type I), the second based on triple-junction thin-film silicon solar cells completely immersed in the electrolyte for thermal coupling (type II) and the last one based on a SHJ mini module

separated from the electrolyzer (type III). For type I, the initial STH efficiency (7%) continuously decreased within 2 h (5.6% after 2 h). The main reason was probably the light induced temperature increase on the PV part. The STH efficiency loss has significantly decreased by immersing the PV part directly in the electrolyte for the type II device. Here the STH efficiency was only slightly decreased from 7.6% to 7.4% within 2 h. Finally, in order to realize a high STH efficiency, we employed a SHJ shingled module with three series-connected cells. Here a stable average STH efficiency of 13.3% was achieved for 2 h.
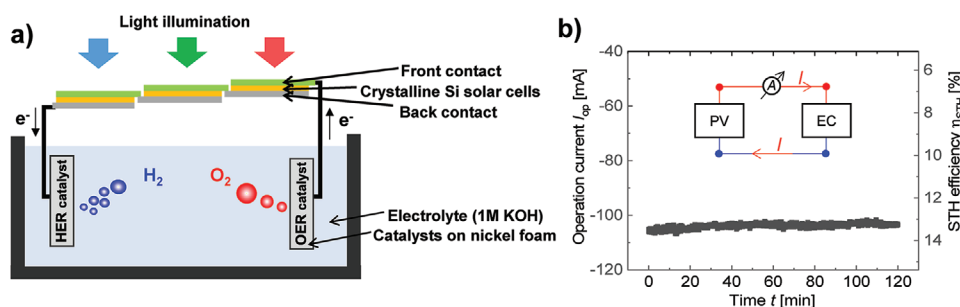

Figure 7. Integrated PV-EC device (type III) consisting of the shingled module (three series-connected SHJ solar cells, total PV area: 9.6 cm²) and the $Co_{0.6}Fe_{0.3}V_{0.1}O_x$ bifunctional catalysts (EC: 120 cm²). a) Schematic illustration of integrated PV-EC device where the shingled module is connected to the $Co_{0.6}Fe_{0.3}V_{0.1}O_x$ bifunctional catalyst with wire. b) Operation current (left y-axis) and the corresponding STH efficiency (right y-axis) of integrated PV-EC device (III) as a function of time under bias-free ($V = 0$ V) conditions. The faradaic efficiency was assumed to be 100%. The experiment was carried out under 1 sun of AM1.5G illumination intensity in 1.0 M KOH at room temperature.

2000592 (7 of 9)

**ADVANCED
SCIENCE NEWS**

www.advancedsciencenews.com

**ADVANCED
MATERIALS
TECHNOLOGIES**

www.advmattechnol.de

4. Experimental Section

Fabrication of Triple-Junction Si Solar Cell: Two different types of triple-junction Si solar cells (a-Si:H/a-Si:H/μc-Si:H and a-Si:H/μc-Si:H/μc-Si:H) were prepared on the F-doped SnO$_2$ (SnO$_2$:F) coated glass (10 × 10 cm^2). All the thin-film Si layers were deposited by means of plasma enhanced chemical vapor deposition (PECVD). A layered stack of Al-doped ZnO and Ag (ZnO:Al/Ag/ZnO:Al) were deposited as back contact through radio frequency magnetron sputtering. More detailed information regarding preparation of thin-film Si solar cells can be found in some of our previous works.[29,32]

Fabrication of Silicon Heterojunction Shingled Mini Module: SHJ solar cells were prepared on n-type double side textured Czochralski (CZ) M2 silicon wafers with the thickness of 170 µm. The wafers were chemically cleaned with RCA Standard Clean 1 (NH$_4$OH: H$_2$O$_2$: deionized water), RCA Standard Clean 2 (HCl: H$_2$O$_2$: deionized water) and subsequently dipped into 1% HF solution for 5 min to remove the surface oxide. Passivating and doped amorphous silicon layers were deposited with PECVD at 200 °C in rear junction configuration. Approximately 90 nm thick indium tin oxide (ITO) layers were deposited with magnetron sputtering on top of thin-film Si-doped layers on both sides of the device. The cells were finalized with Ag screen printed contacts. The mask for screen printing was designed to achieve a number of individual cells with an area of 17 × 21 mm, each with one busbar at the top and bottom side of the device. The cells were cut out of the wafer with laser and characterized individually. After selection the cells were soldered with aid of low temperature soldering paste in shingled configuration to prepare a module with the required number of cells. The bottom busbar of one cell has been soldered to the top busbar of the next cell in the overlapping region. The module was finalized with copper ribbon contacts soldered to the busbars at the edges.

Preparation of Electrocatalyst: In the present study, all mixed metal catalysts were prepared by electrodeposition. A two-electrode electrochemical system was utilized for the electrodeposition where nickel sheet and carbon rod were used as working and counter electrodes, respectively. As shown in Table S2, Supporting Information, five different types of catalysts were prepared under the same conditions based on a different composition ratio. For the preparation of the precursor solution, CoSO$_4$ (Acros Organics, Finland, 99%), FeSO$_4$·7H$_2$O (Sigam-Aldrich, USA, 99%) and VOSO$_4$ (Alfa Aesar, USA, 99.9%) were weighed according to their molar mass. The mixed precursors were added in 200 mL of deionized water. Prior to electrodeposition, Ni sheet was cut into 46 mm x 12 mm pieces and carefully cleaned with diluted hydrochloric acid (3 M HCl), ethanol, and deionized water in an ultrasonic cleaning bath. Subsequently, the substrates were dried in ambient air. At the beginning of electrodeposition, nitrogen was blown into the precursor solution for 10 min to prevent the unexpected oxidation of metal ions in the solution. The electrodeposition was carried out with a potentiostat/galvanostat (Gamry Instruments, Reference 600) applying constant current density of –60 mA cm^{-2} at a temperature of 60 °C. The deposition time was maintained at 1 min for all cases.

Electrochemical Measurements: All measurements were conducted with potentiostats (Gamry Instruments Reference 600, 1010E, and source measure unit) in a three (or two) electrode configuration. Pt foil and Ag/AgCl (3 M KCl) were used as the counter and the reference electrode, respectively. The potential measured with Ag/AgCl reference electrode was converted to a reversible hydrogen electrode (RHE) potential according to the following formula, E (vs RHE) = E (vs Ag/AgCl) + 0.21 + 0.059 V × pH. Notably, no ohmic voltage loss (*iR* drop) was compensated here because such a loss cannot be ruled out in a real PV-EC system. The integrated PV-EC device was measured with an in-house built sun simulator at AM 1.5G (1 sun; 100 mW cm^{-2}, 25 °C) spectrum conditions. The STH efficiency was calculated using Equation (3) assuming a faradaic efficiency of 100%.

$$STH = \left[\frac{I \times (1.23\,V) \times \eta_F}{P_{IN} \times A} \right]_{AM1.5G} \qquad (3)$$

Where I is operation current of the device, E_{thermo} (at 25 °C) = 1.23 V, η_F is the faradaic efficiency, P_{IN} is incident illumination power density (100 mW cm^2), and A is the active area of PV.

Spectroscopy Characterization: XPS measurements were conducted with a MULTIPROBE MXPS system from Scienta Omicron, which is part of the JOSEPH cluster system in the research center Jülich. The system uses an XM 1000 AlKα X-ray source operated at 300 W. The resultant spectra are collected in constant analyzer energy mode with an ARGUS hemispherical electron spectrometer. Path energies of 100 eV for the survey spectrum and 20 eV for the high-resolution spectra were used. Binding energies were referenced to the C 1s peak at 285 eV. Intensities for oxygen and vanadium were determined by measuring the area of each peak, after subtracting a Shirley-type background and fitting the experimental curve to a combination of Lorentzian and Gaussian lines with a fixed proportion of 30:70. Following the procedure given in ref. [22], the spectra of Co 2p and Fe 2p were corrected for the Auger LMM peaks that each metal has in the 2p energy range of the other metal. To perform the correction the ratio of Auger to metal 2p peak area was determined on FeO$_x$ and Co$_6$V$_4$O$_x$ samples treated in the same way as the catalysts. Then the intensities of Co 2p and Fe 2p were determined from the integrated peak area (without a fitting procedure) corrected by the LMM area of the respective other metal. In addition, for the Co 2p and Fe 2p spectra depicted in Figure 3 the scaled signal of the LMM peak of the other element (determined on the reference samples) was subtracted.

The surface state of the samples was investigated using grazing incidence X-ray diffraction (GIXRD, Empyrean (Malvern Panalytical GmbH)) with CuKα radiation (45 kV/ 40 mA). For the investigation of the surface topography and the composition of the samples, a scanning electron microscope (SEM, FEI Magellan 400 at accelerating voltages of 20 kV) equipped with EDX (Oxford X-Max 80 mm²) analysis was carried out.

Supporting Information

Supporting Information is available from the Wiley Online Library or from the author.

Acknowledgements

Conflict of Interest

The authors declare no conflict of interest.

Author Contributions

U.R., F.F., and S.H. developed the conceptual idea and supervised the work. M.L. and X.D. designed and conducted the experiment, and prepared a draft of the manuscript. S.B., F.K., V.S., O.A., T.M., B.K., and T.K. performed the experimental measurements and analysis. All the authors discussed the results and commented on the manuscript.

2000592 (8 of 9)

[1] N. S. Lewis, *Science* **2016**, *351*, aad1920.

[2] a) N. S. Lewis, D. G. Nocera, *Proc. Natl. Acad. Sci. U. S. A.* **2006**, *103*, 15729; b) M. G. Walter, E. L. Warren, J. R. McKone, S. W. Boettcher, Q. Mi, E. A. Santori, N. S. Lewis, *Chem. Rev.* **2010**, *110*, 6446; c) T. R. Cook, D. K. Dogutan, S. Y. Reece, Y. Surendranath, T. S. Teets, D. G. Nocera, *Chem. Rev.* **2010**, *110*, 6474.

[3] S. A. Elmquist, P. Weber, H. Eichberger, *Stahl Eisen* **2002**, *122*, 59.

[4] a) Q. Wang, K. Domen, *Chem. Rev.* **2020**, *120*, 919; b) Z. Wang, C. Li, K. Domen, *Chem. Soc. Rev.* **2019**, *48*, 2109.

[5] a) C. Jiang, S. J. A. Moniz, A. Wang, T. Zhang, J. Tang, *Chem. Soc. Rev.* **2017**, *46*, 4645; b) Z.-Q. Wei, X.-C. Dai, S. Hou, Y.-B. Li, M.-H. Huang, T. Li, S. Xu, F.-X. Xiao, *J. Mater. Chem. A* **2020**, *8*, 177; c) S. Hou, X.-C. Dai, Y.-B. Li, M.-H. Huang, T. Li, Z.-Q. Wei, Y. He, G. Xiao, F.-X. Xiao, *J. Mater. Chem. A* **2019**, *7*, 22487; d) X.-C. Dai, M.-H. Huang, Y.-B. Li, T. Li, B.-B. Zhang, Y. He, G. Xiao, F.-X. Xiao, *J. Mater. Chem. A* **2019**, *7*, 2741.

[6] J. H. Kim, D. Hansora, P. Sharma, J.-W. Jang, J. S. Lee, *Chem. Soc. Rev.* **2019**, *48*, 1908.

[7] a) M. Reuß, J. Reul, T. Grube, M. Langemann, S. Calnan, M. Robinius, R. Schlatmann, U. Rau, D. Stolten, *Sustainable Energy Fuels* **2019**, *3*, 801; b) T. J. Jacobsson, V. Fjällström, M. Edoff, T. Edvinsson, *Energy Environ. Sci.* **2014**, *7*, 2056; c) T. J. Jacobsson, V. Fjällström, M. Edoff, T. Edvinsson, *Sol. Energy Mater. Sol. Cells* **2015**, *134*, 185; d) J. W. Ager, M. R. Shaner, K. A. Walczak, I. D. Sharp, S. Ardo, *Energy Environ. Sci.* **2015**, *8*, 2811; e) S. Ardo, D. Fernandez Rivas, M. A. Modestino, V. Schulze Greiving, F. F. Abdi, E. Alarcon Llado, V. Artero, K. Ayers, C. Battaglia, J.-P. Becker, D. Bederak, A. Berger, F. Buda, E. Chinello, B. Dam, V. Di Palma, T. Edvinsson, K. Fujii, H. Gardeniers, H. Geerlings, S. M. H. Hashemi, S. Haussener, F. Houle, J. Huskens, B. D. James, K. Konrad, A. Kudo, P. P. Kunturu, D. Lohse, B. Mei, et al., *Energy Environ. Sci.* **2018**, *11*, 2768.

[8] a) F. Song, L. Bai, A. Moysiadou, S. Lee, C. Hu, L. Liardet, X. Hu, *J. Am. Chem. Soc.* **2018**, *140*, 7748; b) N. Mahmood, Y. Yao, J.-W. Zhang, L. Pan, X. Zhang, J.-J. Zou, *Adv. Sci.* **2018**, *5*, 1700464.

[9] J. Wang, W. Cui, Q. Liu, Z. Xing, A. M. Asiri, X. Sun, *Adv. Mater.* **2016**, *28*, 215.

[10] a) N. Xu, J. A. Wilson, Y.-D. Wang, T. Su, Y. Wei, J. Qiao, X.-D. Zhou, Y. Zhang, S. Sun, *Appl. Catal., B* **2020**, *272*, 118953; b) N. Xu, Q. Nie, J. Liu, H. Huang, J. Qiao, X.-D. Zhou, *J. Electrochem. Soc.* **2020**, *167*, 050512.

[11] a) M. S. Burke, M. G. Kast, L. Trotochaud, A. M. Smith, S. W. Boettcher, *J. Am. Chem. Soc.* **2015**, *137*, 3638; b) P. Babar, A. Lokhande, H. H. Shin, B. Pawar, M. G. Gang, S. Pawar, J. H. Kim, *Small* **2018**, *14*, 1702568; c) B. Zhang, H. Wang, Z. Zuo, H. Wang, J. Zhang, *J. Mater. Chem. A* **2018**, *6*, 15728; d) S.-F. Hung, Y. Zhu, G.-Q. Tzeng, H.-C. Chen, C.-S. Hsu, Y.-F. Liao, H. Ishii, N. Hiraoka, H. M. Chen, *ACS Energy Lett.* **2019**, *4*, 2813.

[12] a) L. Liardet, X. Hu, *ACS Catal.* **2018**, *8*, 644; b) J. Liu, Y. Ji, J. Nai, X. Niu, Y. Luo, L. Guo, S. Yang, *Energy Environ. Sci.* **2018**, *11*, 1736.

[13] a) K. Chakrapani, G. Bendt, H. Hajiyani, T. Lunkenbein, M. T. Greiner, L. Masliuk, S. Salamon, J. Landers, R. Schlögl, H. Wende, R. Pentcheva, S. Schulz, M. Behrens, *ACS Catal.* **2018**, *8*, 1259; b) Y. Hu, Z. Wang, W. Liu, L. Xu, M. Guan, Y. Huang, Y. Zhao, J. Bao, H.-M. Li, *ACS Sustainable Chem. Eng.* **2019**, *7*, 16828.

[14] a) N. Han, K. R. Yang, Z. Lu, Y. Li, W. Xu, T. Gao, Z. Cai, Y. Zhang, V. S. Batista, W. Liu, X. Sun, *Nat. Commun.* **2018**, *9*, 924; b) F. Yu, H. Zhou, Y. Huang, J. Sun, F. Qin, J. Bao, W. A. Goddard, S. Chen, Z. Ren, *Nat. Commun.* **2018**, *9*, 2551; c) A.-L. Wang, H. Xu, G.-R. Li, *ACS Energy Lett.* **2016**, *1*, 445; d) F. Qin, Z. Zhao, M. K. Alam, Y. Ni, F. Robles-Hernandez, L. Yu, S. Chen, Z. Ren, Z. Wang, J. Bao, *ACS Energy Lett.* **2018**, *3*, 546; e) M. I. Jamesh, *J. Power Sources* **2016**, *333*, 213; f) J. R. McKone, S. C. Marinescu, B. S. Brunschwig, J. R. Winkler, H. B. Gray, *Chem. Sci.* **2014**, *5*, 865; g) B. M. Hunter, H. B. Gray, A. M. Müller, *Chem. Rev.* **2016**, *116*, 14120; h) X. Lu, C. Zhao, *Nat. Commun.* **2015**, *6*, 6616.

[15] C. G. Morales-Guio, L. Liardet, X. Hu, *J. Am. Chem. Soc.* **2016**, *138*, 8946.

[16] M. A. Ehsan, A. S. Hakeem, M. Sharif, A. Rehman, *ACS Omega* **2019**, *4*, 12671.

[17] a) K. Lohrberg, P. Kohl, *Electrochim. Acta* **1984**, *29*, 1557; b) B.-Q. Li, Z.-J. Xia, B. Zhang, C. Tang, H.-F. Wang, Q. Zhang, *Nat. Commun.* **2017**, *8*, 934; c) D. Xu, M. B. Stevens, Y. Rui, G. DeLuca, S. W. Boettcher, E. Reichmanis, Y. Li, Q. Zhang, H. Wang, *Electrochim. Acta* **2018**, *265*, 10.

[18] J. K. Nørskov, T. Bligaard, J. Rossmeisl, C. H. Christensen, *Nat. Chem.* **2009**, *1*, 37.

[19] a) H. Dau, C. Limberg, T. Reier, M. Risch, S. Roggan, P. Strasser, *ChemCatChem* **2010**, *2*, 724; b) F. Dionigi, P. Strasser, *Adv. Energy Mater.* **2016**, *6*, 1600621.

[20] J. O. M. Bockris, T. Otagawa, *J. Electrochem. Soc.* **1984**, *131*, 290.

[21] a) J. P. Singh, T. M. Lu, G. C. Wang, *Appl. Phys. Lett.* **2003**, *82*, 4672; b) C. Spöri, J. T. H. Kwan, A. Bonakdarpour, D. P. Wilkinson, P. Strasser, *Angew. Chem., Int. Ed.* **2017**, *56*, 5994; c) M. Lee, H. S. Jeon, S. Y. Lee, H. Kim, S. J. Sim, Y. J. Hwang, B. K. Min, *J. Mater. Chem. A* **2017**, *5*, 19210; d) M. Lee, B. Turan, J.-P. Becker, K. Welter, B. Klingebiel, E. Neumann, Y. J. Sohn, T. Merdzhanova, T. Kirchartz, F. Finger, U. Rau, S. Haas, *Adv. Sustainable Syst.* **2020**, *4*, 2000070; e) M. Lee, H.-S. Oh, M. K. Cho, J.-P. Ahn, Y. J. Hwang, B. K. Min, *Appl. Catal., B* **2018**, *233*, 130; f) M. Lee, M. S. Jee, S. Y. Lee, M. K. Cho, J.-P. Ahn, H.-S. Oh, W. Kim, Y. J. Hwang, B. K. Min, *ACS Appl. Mater. Interfaces* **2018**, *10*, 24499.

[22] P. M. Kouotou, H. Vieker, Z. Y. Tian, P. H. T. Ngamou, A. El Kasmi, A. Beyer, A. Gölzhäuser, K. Kohse-Höinghaus, *Catal. Sci. Technol.* **2014**, *4*, 3359.

[23] a) J. Mendialdua, R. Casanova, Y. Barbaux, *J. Electron Spectrosc. Relat. Phenom.* **1995**, *71*, 249; b) K. Fan, H. Chen, Y. Ji, H. Huang, P. M. Claesson, Q. Daniel, B. Philippe, H. Rensmo, F. Li, Y. Luo, L. Sun, *Nat. Commun.* **2016**, *7*, 11981.

[24] H. Michibata, *Vanadium: Biochemical and Molecular Biological Approaches*, Springer, Berlin **2012**.

[25] https://www.surfgroup.be/semedx (accessed: September 2020).

[26] https://www.phi.com/surface-analysis-techniques/xps-esca.html (accessed: September 2020).

[27] T. Shinagawa, K. Takanabe, *ChemSusChem* **2017**, *10*, 1318.

[28] Z. Xing, H. Wu, L. Wu, X. Wang, H. Zhong, F. Li, J. Shi, D. Song, W. Xiao, C. Jiang, F. Ren, *J. Mater. Chem. A* **2018**, *6*, 21167.

[29] F. Urbain, V. Smirnov, J.-P. Becker, A. Lambertz, F. Yang, J. Ziegler, B. Kaiser, W. Jaegermann, U. Rau, F. Finger, *Energy Environ. Sci.* **2016**, *9*, 145.

[30] F. Urbain, J.-P. Becker, V. Smirnov, J. Ziegler, F. Yang, B. Kaiser, W. Jaegermann, S. Hoch, A. Maljusch, U. Rau, F. Finger, *Mater. Sci. Semicond. Process.* **2016**, *42*, 142.

[31] a) L. Wang, X. Huang, S. Jiang, M. Li, K. Zhang, Y. Yan, H. Zhang, J. M. Xue, *ACS Appl. Mater. Interfaces* **2017**, *9*, 40281; b) C. Meng, B. Wang, Z. Gao, Z. Liu, Q. Zhang, J. Zhai, *Sci. Rep.* **2017**, *7*, 41825; c) K. Wang, C. Liao, W. Wang, Y. Xiao, X. Liu, Y. Zuo, *ACS Appl. Energy Mater.* **2020**, *3*, 6752.

[32] a) J. P. Becker, B. Turan, V. Smirnov, K. Welter, F. Urbain, J. Wolff, S. Haas, F. Finger, *J. Mater. Chem. A* **2017**, *5*, 4818; b) B. Turan, J.-P. Becker, F. Urbain, F. Finger, U. Rau, S. Haas, *Nat. Commun.* **2016**, *7*, 12681.

[33] F. Dinkel, *B.S. Thesis*, Technische Hochschule Köln, Cologne **2018**.